Volume 25
Number 4
28 January 2023
Pages 499–694

CrystEngComm

rsc.li/crystengcomm

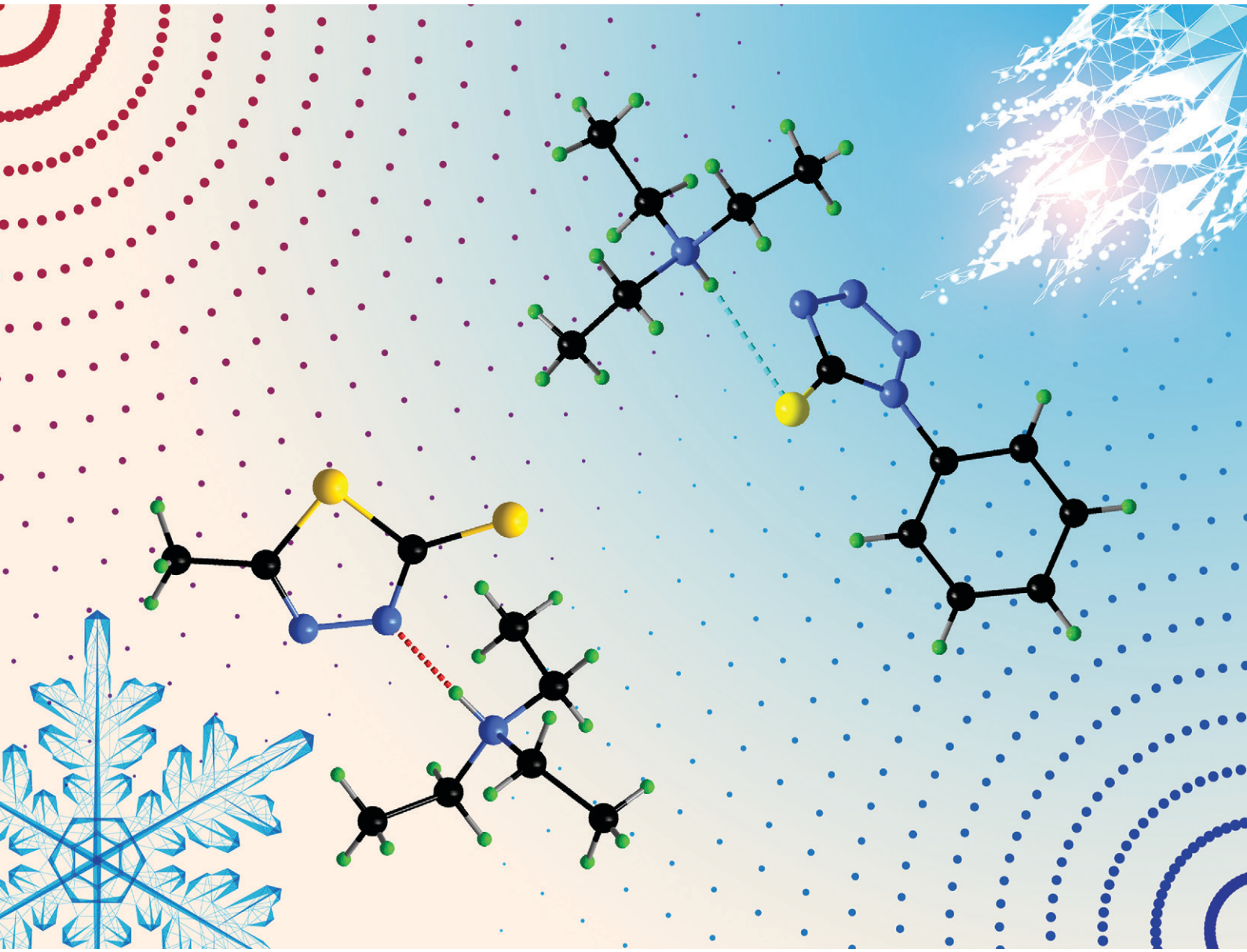

ISSN 1466-8033

ROYAL SOCIETY OF CHEMISTRY

PAPER

Anja-Verena Mudring, Robin D. Rogers *et al.*
Investigation of the role of hydrogen bonding in ionic liquid-like salts with both N- and S-soft donors

CrystEngComm

PAPER

View Article Online
View Journal | View Issue

Cite this: *CrystEngComm*, 2023, **25**, 530

Investigation of the role of hydrogen bonding in ionic liquid-like salts with both N- and S-soft donors†

Olivier Renier, [a] Guillaume Bousrez, [a] Volodymyr Smetana, [a] Anja-Verena Mudring *[ab] and Robin D. Rogers *[ac]

Received 11th July 2022,
Accepted 4th October 2022

DOI: 10.1039/d2ce00961g

rsc.li/crystengcomm

In search of ionic liquids (ILs) with multiple types of soft donor atoms capable of preferentially complexing a range of soft metal ions over harder ions, we investigated structural clues to the role of hydrogen bonding in IL behavior through a series of salts with anions containing both N- and S-donor atoms based on azole thiolates. Reaction of equimolar amounts of triethylamine (Et_3N) or diisobutylamine (DBA) with 1-phenyl-1*H*-tetrazole-5-thiol (PhTzSH), 1-methyl-1*H*-tetrazole-5-thiol (MeTzSH), or 5-methyl-1,3,4-dithiazole-2-thiol (MeDiTSH) yielded [Et_3NH][MeTzS] (**1**), a yellow liquid, and the low melting yellow solids [DBAH][MeTzS] (**2**), [Et_3NH][PhTzS] (**3**), [DBAH][PhTzS] (**4**), [Et_3NH][MeDiTS] (**5**), and [DBAH][MeDiTS] (**6**). Thermal analysis revealed that all of them qualify as ILs with melting points below 100 °C. Single crystal X-ray structure analysis of **2**–**6** revealed the presence of an extensive H-bonding network that includes the rare N–H···S hydrogen bonds in **3**, **4**, and **6**. These weaker interactions appear to significantly influence thermal behavior, where strong bonding leads to higher melting temperatures and lower decomposition points.

1. Introduction

Separations involving f-elements are currently of considerable interest in a variety of fields including nuclear chemistry,[1,2] environmental remediation,[3] and recovery of lanthanides from electronic waste.[4,5] The separation of f-elements is extremely difficult and finding an easy and cheap method to achieve this is becoming ever more important as they are key constituents in materials for energy efficient applications such as in magnets for wind turbines and e-vehicles as well as consumer-related.[6–8] This is particularly true for separations of heavier 5f-elements from 4f-elements in nuclear waste remediation, where although both hard donor complexants will sometimes work; the softer donor complexants have been used to separate transuranic elements from their lanthanide analogs.[2] Controlling the number and type of soft donor atoms in a given complexant may offer the possibility to selectively extract 4f- from 5f-metals or *vice versa*.[9–14]

We and others have explored a range of new f-element separations using ionic liquids (ILs) as both solvents and complexants.[4,15,16] ILs can easily accommodate many desired functionalities separately on their cationic and anionic parts or jointly on a given ion while still allowing additional chemical tuning towards the required physical properties of a given separation (melting point, density, viscosity, *etc.*).[17] While there have been many studies to tune IL physical properties for separation, there have been comparatively few which have focused on tuning the hard/soft donor balance needed to execute separations of lanthanides and actinides, which have similar hardness.[18]

To begin to build a library of soft donor salts and learn more about features of mixed soft donor anions that would be amenable to forming low melting salts, we began this study of thiolate anions formed by deprotonation of 1-phenyl-1*H*-tetrazole-5-thiol (PhTzSH), 1-methyl-1*H*-tetrazole-5-thiol (MeTzSH), and 5-methyl-1,3,4-dithiazole-2-thiol (MeDiTSH).

In general, thiolate ILs have rarely been investigated and little is known about their intra- and intermolecular interactions. Azole thiols present the extra advantage of containing two soft donor atoms, sulfur and nitrogen,[19]

[a] *Department of Materials and Environmental Chemistry, Stockholm University, 10691 Stockholm, Sweden. E-mail: mudring@iastate.edu*
[b] *Department of Chemistry and iNANO, 253 Aarhus University, 8000 Aarhus C, Denmark*
[c] *Department of Chemistry & Biochemistry, The University of Alabama, Tuscaloosa, AL 35487, USA. E-mail: rdrogers@ua.edu*

† Electronic supplementary information (ESI) available: Experimental details, instrumentation, ^{1}H and ^{13}C NMR spectra, FTIR spectra, TG and DSC curves, PXRD diffractograms, SCXRD details, and POM images. CCDC 2084096–2084100 contain the supplementary crystallographic data for this paper. For ESI and crystallographic data in CIF or other electronic format see DOI: **https://doi.org/10.1039/d2ce00961g**

which can further be exploited towards metal-specific interactions.[20] The complexation of Hg(II) *via* the sulfur atom by some derivatives such as the 5-mercapto-1-methyltetrazole has been reported,[21,22] while the presence of nitrogen as a second soft donor could promote the complexation of other metal classes such as f-elements. Thiols in hydrophobic ILs have also been recommended as potential ligands to extract toxic heavy metals.[23–26]

We hypothesized that these types of ILs could be better understood and designed following the approach of anti-crystal engineering, *i.e.*, by the deliberate avoidance of any structural features that favor interaction between cation and anion and thus intricate crystallization.[27,28] For this purpose, a series of salts with two small amines, triethylamine (Et_3N) and diisobutylamine (DBA), was prepared and structurally characterized. Binary and ternary amine cations have been involved to evaluate the H-bonding factor and compare their ability to yield crystalline salts. Here, we report our initial results obtained by simple acid/base reactions of MeTzSH, PhTzSH, and MeDiTSH with Et_3N and DBA.

2. Experimental section

2.1 Chemicals and materials

Triethylamine (Et_3N, ≥99.5%), diisobutylamine (DBA, 99%), 5-mercapto-1-methyltetrazole (MeTzSH 98%), 1-phenyl-1*H*-tetrazole-5-thiol (PhTzSH, 98%), 5-methyl-1,3,4-dithiazole-2-thiol (MeDiTSH, 99%) and methanol (99.8%) were all purchased from Sigma-Aldrich (Steinheim, Germany) or Alfa Aesar (Karlsruhe, Germany). Et_3N and DBA were distilled over KOH before use.

2.2 Synthesis

The respective amine (10 mmol, 1.0 eq.) and MeTzSH, PhTzSH, or MeDiTSH (10 mmol, 1.0 eq.) were added together with 20 mL of CH_3OH (20 mL) in a 100 mL round bottom flask. The mixture was heated under reflux for 4 h and cooled to room temperature. The solvent was removed at 40 °C under reduced pressure using a rotary evaporator to yield the final product in quantitative yield. Single crystals suitable for single crystal X-ray diffraction (SCXRD) analyses were obtained by isothermal evaporation of dilute methanolic (**2**–**4**) or ethyl acetate (**5**–**6**) solutions.

[Et_3NH][MeTzS] (**1**): Yellow oil. ^{1}H NMR (400 MHz, DMSO-d_6): 1.19 (t, J_{H-H} = 7.2 Hz, 9H), 3.12 (q, J_{H-H} = 14.8 Hz, J_{H-H} = 7.2 Hz, 6H), 3.66 (s, 3H). ^{13}C NMR (100 MHz, DMSO-d_6): 8.6, 32.6, 45.8, 167.1. ν_{max} (cm^{-1}): 2981, 2945, 2885, 2463, 1451, 1427, 1353, 1275, 1260, 1212, 1160, 1082, 1034, 967, 898, 836, 808, 792, 705, 553, 536, 519, 498, 466, 418. ESI TOF *m*/*z* (positive mode) 102.1041 (calculated *m*/*z* = 102.1283). ESI TOF *m*/*z* (negative mode) 114.9359 (calculated *m*/*z* = 115.0078). T_{glass} = −57 °C; T_{decomp} = 164 °C.

[DBAH][MeTzS] (**2**): Yellow solid. ^{1}H NMR (400 MHz, DMSO-d_6): 0.90 (d, J_{H-H} = 6.4 Hz, 12H), 2.02 (hept, J_{H-H} = 20.4 Hz, J_{H-H} = 13.6 Hz, J_{H-H} = 6.8 Hz, 2H), 2.84 (d, J_{H-H} = 7.2 Hz, 4H), 3.66 (s, 3H), 8.60 (bs, 2H). ^{13}C NMR (100 MHz, DMSO-d_6): 20.1, 25.1, 32.6, 54.6, 167.3. ν_{max} (cm^{-1}): 3004, 2964, 2872, 2788, 2557, 2452, 1626, 1464, 1425, 1404, 1392, 1357, 1271, 1167, 1105, 1020, 973, 877, 839, 805, 708, 518, 460, 425. ESI TOF *m*/*z* (positive mode) 130.1221 (calculated *m*/*z* = 130.1596). ESI TOF *m*/*z* (negative mode) 114.9359 (calculated *m*/*z* = 115.0078). T_{melt} = 95 °C; T_{cryst} = 38 °C; T_{decomp} = 118 °C.

[Et_3NH][PhTzS] (**3**): Yellow solid. ^{1}H NMR (400 MHz, DMSO-d_6): 1.17 (t, J_{H-H} = 7.2 Hz, 9H), 3.12 (q, J_{H-H} = 14.4 Hz, J_{H-H} = 7.2 Hz, 6H), 7.38 (t, J_{H-H} = 7.2 Hz, 1H), 7.50 (t, J_{H-H} = 8.0 Hz, 2H), 8.02 (d, J_{H-H} = 8.0 Hz, 2H). ^{13}C NMR (100 MHz, DMSO-d_6): 8.5, 45.8, 123.5, 127.4, 128.5, 136.6, 167.0. ν_{max} (cm^{-1}): 2985, 2944, 2631, 2474, 1593, 1493, 1466, 1434, 1412, 1376, 1350, 1309, 1287, 1261, 1213, 1162, 1113, 1081, 1062, 1037, 1010, 987, 921, 896, 836, 809, 769, 737, 720, 693, 684, 613, 567, 535, 509, 455, 413. ESI TOF *m*/*z* (positive mode) 102.1041 (calculated *m*/*z* = 102.1283). ESI TOF *m*/*z* (negative mode) 176.9084 (calculated *m*/*z* = 177.0235). T_{melt} = 79 °C; T_{glass} = −40 °C; T_{decomp} = 135 °C.

[DBAH][PhTzS] (**4**): Yellow solid. ^{1}H NMR (400 MHz, DMSO-d_6): 0.92 (d, J_{H-H} = 6.4 Hz, 12H), 2.01 (hept, J_{H-H} = 20.4 Hz, J_{H-H} = 13.6 Hz, J_{H-H} = 6.8 Hz, 2H), 2.81 (d, J_{H-H} = 7.2 Hz, 4H), 7.37 (t, J_{H-H} = 7.2 Hz, 1H), 7.49 (t, J_{H-H} = 8.0 Hz, 2H), 8.03 (d, J_{H-H} = 7.6 Hz, 2H), 8.43 (bs, 2H). ^{13}C NMR (100 MHz, DMSO-d_6): 20.0, 25.1, 54.5, 123.4, 127.3, 128.4, 136.7, 167.1. ν_{max} (cm^{-1}): 2959, 2875, 2759, 2541, 2438, 1596, 1498, 1466, 1408, 1373, 1352, 1329, 1309, 1285, 1208, 1173, 1159, 1079, 1065, 1042, 1015, 964, 934, 909, 877, 838, 807, 760, 717, 693, 682, 563, 519, 459, 426. ESI TOF *m*/*z* (positive mode) 130.1221 (calculated *m*/*z* = 130.1596). ESI TOF *m*/*z* (negative mode) 176.9084 (calculated *m*/*z* = 177.0235). T_{melt} = 98 °C; T_{glass} = −15 °C; T_{decomp} = 134 °C.

[Et_3NH][MeDiTS] (**5**): Yellow solid. ^{1}H NMR (400 MHz, DMSO-d_6): 1.18 (t, J_{H-H} = 7.2 Hz, 9H), 2.42 (s, 3H), 3.10 (q, J_{H-H} = 14.4 Hz, J_{H-H} = 7.2 Hz, 6H). ^{13}C NMR (100 MHz, DMSO-d_6): 8.7, 15.8, 45.7, 159.4, 187.4. ν_{max} (cm^{-1}): 3451, 3038, 2976, 2855, 2708, 2647, 1702, 1553, 1463, 1447, 1377, 1308, 1266, 1196, 1173, 1129, 1050, 1025, 970, 836, 761, 737, 656, 621, 584, 537, 430. ESI TOF *m*/*z* (positive mode) 102.1041 (calculated *m*/*z* = 102.1283). ESI TOF *m*/*z* (negative mode) 131.1935 (calculated *m*/*z* = 130.9738). T_{melt} = 34 °C; T_{glass} = −41 °C; T_{decomp} = 164 °C.

[DBAH][MeDiTS] (**6**): Yellow solid. ^{1}H NMR (400 MHz, DMSO-d_6): 0.92 (d, J_{H-H} = 6.4 Hz, 12H), 1.94–2.00 (m, 2H), 2.39 (s, 3H), 2.77–2.80 (m, 4H). ^{13}C NMR (100 MHz, DMSO-d_6): 15.6, 20.2, 25.3, 54.6, 158.9, 185.9. ν_{max} (cm^{-1}): 3041, 2957, 2869, 2803, 2753, 2711, 2654, 2525, 2396, 2334, 1554, 1464, 1449, 1402, 1392, 1378, 1329, 1314, 1270, 1192, 1174, 1132, 1075, 1065, 1047, 1030, 1007, 965, 927, 857, 804, 756, 742, 653, 623, 611, 586, 538, 520, 462, 432. ESI TOF *m*/*z* (positive mode) 130.1221 (calculated *m*/*z* = 130.1596). ESI TOF *m*/*z* (negative mode) 131.1935 (calculated *m*/*z* = 130.9738). T_{melt} = 95 °C; T_{cryst} = 90 °C; T_{decomp} = 169 °C.

2.3 Instrumentation

^{1}H and ^{13}C nuclear magnetic resonance (NMR) spectra were recorded at room temperature in DMSO on a Bruker 400

MHz spectrometer equipped with a BBO probe (Bruker, Ettlingen, Germany). Chemical shifts are reported in delta (δ) units, expressed in parts per million (ppm). The following abbreviations were used for the observed multiplicities: s (singlet), d (doublet), t (triplet), q (quartet), hept (heptuplet), br (broad), m (multiplet for unresolved lines). ^{1}H NMR chemical shifts were referenced to the residual solvent signal for DMSO (2.50 ppm), and ^{13}C NMR chemical shifts were referenced to the solvent signal of DMSO (39.52 ppm).

Fourier transform infrared spectroscopy (FTIR) was conducted with a Bruker Alpha-P ATR-spectrometer (Bruker, Ettlingen, Germany) in attenuated total reflection configuration. The data evaluation was carried out with the program OPUS (Bruker, Ettlingen, Germany).

Differential scanning calorimetry (DSC) was performed with a computer-controlled Phoenix DSC 204 F1 thermal analyzer (Netzsch, Selb, Germany). The samples were placed in aluminum pans (in air), which were cold-sealed and punctured. Before recording the DSC thermogram, the samples were cooled to −60 °C. Measurements were carried out at a heating rate of 5 °C min^{-1} under nitrogen flow (40 mL min^{-1}). Given temperatures correspond to the onset of the respective thermal process. Given temperatures of glass transition correspond to the midpoint.

Thermogravimetric analysis (TGA) was performed with a TG 449 F3 Jupiter (Netzsch, Selb, Germany). Samples were placed under ambient atmosphere in aluminum oxide crucibles for the measurements. Measurements were carried out with a heating rate of 10 °C min^{-1} and air as the purge gas. Given temperatures correspond to a 5% onset.

Optical analyses were made by heated-stage polarized optical microscopy (POM) with an Axio Imager A1 microscope (Carl Zeiss MicroImaging GmbH, Göttingen, Germany) equipped with a hot stage, THMS600 (Linkam Scientific Instruments Ltd, Surrey, United Kingdom), and Linkam TMS 94 temperature controller (Linkam Scientific Instruments Ltd, Surrey, United Kingdom). Images were recorded at a magnification of 100× as a video with a digital camera. During heating and cooling, the sample was placed between two cover slips. Heating and cooling rates were 5 °C min^{-1}.

A SYNAPT G2-S HDMS Q-ToF mass spectrometer (Waters, Manchester, United Kingdom), with an ESI operated in the positive and negative ion mode, was used in this study. For the measurement, the ion source was operated with a capillary voltage of 2500 V, extractor voltage: 1.0 V, RF lens: 0.5 V, ion source temperature of 120 °C, and desolvation temperature 250 °C. Nitrogen was used as both the cone and desolvation gas at a flow of 70 L h^{-1} and 500 L h^{-1}, respectively. Argon was used as a collision gas at a pressure of 2.95×10^{-4} mbar.

Single crystal X-ray diffraction (SCXRD) data were collected on a Bruker Venture diffractometer (Bruxer AXS, Karlsruhe, Germany) using CuKα radiation (λ = 1.54178 Å at 100 K) or MoKα (λ = 0.71073 Å at 100 K). The crystal structures were solved and refined with SHELXT[29] and SHELXL[30] subroutines within the APEX3[31] software package. Absorption corrections were carried out with the program SADABS.[32] Hydrogen atoms for all structures were calculated geometrically and treated with the riding atom mode. The positional disorder of the C12′ position (split) in **6** has been refined, yielding practically equivalent occupations (0.54/0.46(2)). Illustrations were prepared in Diamond[33] and calculated diffractograms were obtained using Mercury.[34]

Powder X-ray diffraction (PXRD) data were recorded at ambient temperature on a PANalytical X'pert PRO diffractometer (Malvern Panalytical, Malvern, United Kingdom), operating at 45 kV and 40 mA and using CuKα_1 radiation. The data were recorded in reflection mode from 5° to 70° with a step size of 0.01° for 60 min. The detector was a PIXcel3D (Malvern Panalytical, Malvern, United Kingdom) solid-state hybrid pixel detector.

Hirshfeld surfaces and images were calculated and produced using CrystalExplorer17.[35]

3. Results and discussion

3.1 Synthesis

Synthesis. Six salts were prepared by the straightforward acid/base reaction of equimolar amounts of triethylamine (Et_3N) or diisobutylamine (DBA) with 1-phenyl-1*H*-tetrazole-5-thiol (PhTzSH), 1-methyl-1*H*-tetrazole-5-thiol (MeTzSH), or 5-methyl-1,3,4-dithiazole-2-thiol (MeDiTSH) in methanol (Scheme 1). After removal of the solvent under vacuum [Et_3NH][MeTzS] (**1**) was obtained as a yellow liquid whilst [DBAH][MeTzS] (**2**), [Et_3NH][PhTzS] (**3**), [DBAH][PhTzS] (**4**), [Et_3NH][MeDiTS] (**5**), and [DBAH][MeDiTS] (**6**) were obtained as yellow solids. Crystals of **2–4** and **5–6** were obtained by isothermal evaporation of methanolic or ethyl acetate solutions, respectively. The purities of **1–6** were confirmed by ^{1}H and ^{13}C NMR measured in DMSO-d_6 (see ESI† Fig. S1–S12), FTIR (Fig. S13–S18†), ESI-MS, and PXRD (Fig. S42–S46†) for **2–6**. TGA (Fig. S25–S30†), FTIR, and SCXRD analyses confirmed the products were anhydrous salts.

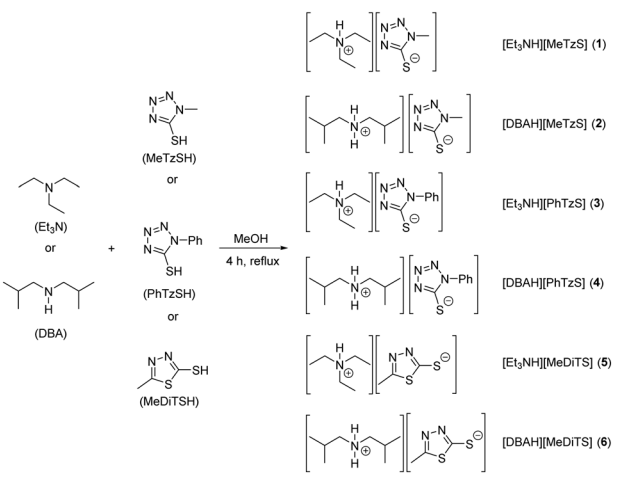

Scheme 1 Synthetic procedures for **1–6**.

3.2 Thermal analyzes

Differential scanning calorimetry (DSC). The six salts were examined with respect to their thermal behavior with DSC and thermogravimetric analysis (TGA), as well as temperature-dependent polarized optical microscopy (POM) to identify the different phase transitions, *vide supra* for experimental details. DSC traces of **1–6** for a complete thermal cycle are presented in Fig. 1. The heating cycles are presented in the top part while the cooling in the bottom part. Detailed graphical representations of DSC traces for all compounds can be found in Fig. S19–S24.†

The DSC data indicate that all six salts meet the definition of an IL with melting points below 100 °C, ranging from the room temperature liquid **1** with T_g = −56.9 °C (Table 1) to T_m = 33.8–98.3 °C for **2–6**. Crystallization of **1** could not be achieved, but an estimation according to $T_m = 1.5\ T_g$ (K)[36] yields T_m = 51.2 °C. Upon cooling, **2** re-crystallizes, albeit with significant supercooling of 67.2 °C. The salts **3–5**, once molten, do not crystallize upon cooling, but exhibit strong super cooling and vitrification way below room temperature – a thermal behavior, which is often found for ILs.[36,37] Compound **6** with melting upon heating and crystallization upon cooling shows similar thermal behavior to compound **2**, albeit with a much lower degree of supercooling (8.4 °C).

The thermal stabilities of the six salts were investigated by thermogravimetric analysis (TGA) from 25 °C to 500 °C under air with a thermal ramp of 10 °C min^{-1} (Fig. 2 and S25–S30†). The 5% onset of decomposition temperatures ($T_{5\%onset}$) are provided in Table 1. **1** slowly loses some mass almost immediately upon heating and exhibits $T_{5\%onset}$ at 164 °C, degrading in one rather broad step ending at 332 °C. **2** is stable till 110 °C and loses almost 90% of its mass in a single step from 122 °C to 200 °C. A second mass loss starts at 210 °C until a total mass loss at 250 °C. Both **3** and **4** are stable until 110 °C, but then slowly decompose until 126 °C and 127 °C, respectively. From there, they both lose around 60% mass until 200 °C and then slowly continue their decomposition process until the end of the measurement, which could contain multiple decomposition steps, where less than 10% of the mass remains. **5** has a small mass loss at the beginning of the measurement, likely to be a minute amount of residual methanol, and then is stable until its decomposition temperature at 164 °C. In about 50 °C, the compound is fully decomposed. **6** decomposes in two well-defined steps, the first step at 82 °C and the second step at 169 °C. A third of the mass is lost in the first step, which can also be observed in DSC (for the first heating trace, the heating content is 6.26 J g^{-1}, and for the second one, the value is 4.28 J g^{-1}). After the second step, the compound is fully decomposed.

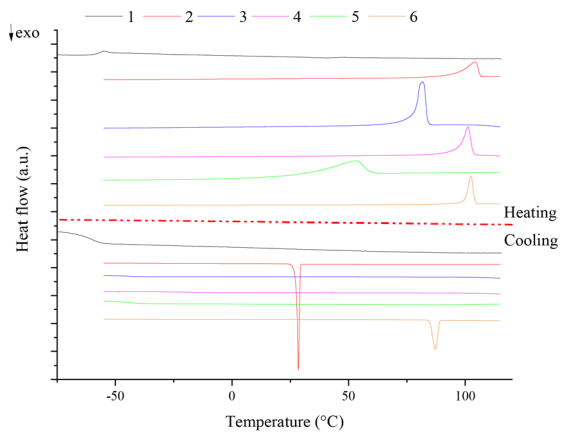

Fig. 1 DSC traces for compounds **1–6**.

All the six salts have $T_{5\%onset}$ values between 122 and 169 °C (Table 1). Interestingly, the only liquid, **1**, has one of the highest $T_{5\%onset}$ values of 164 °C, while **2**, with one of the higher melting points (97.0 °C), has the lowest $T_{5\%onset}$ of 122 °C. These two compounds have the same anion ([MeTzS]$^-$), suggesting that, in this case, the cation has an important impact on the stability of the product. This contrasts with the thermal behavior of **3** and **4**, which have the same anion ([PhTzS]$^-$) with different cations, but the decomposition curves are very similar.

5 and **6**, [MeDiTS]$^-$ salts, have different decomposition curves, but they are fully decomposed around the same temperature (210 °C), suggesting the cation/anion interactions play some role in the mechanism of decomposition. **6**, with [DBAH]$^+$ as the cation, exhibits a two-step decomposition (Fig. S30†), the first step roughly corresponding to the loss of the two isopropyl groups from the cation (32.7% mass loss (experimental) *vs.* 33.0% (theoretical) in the first step). The second step leads to complete decomposition.

The observed results cannot be directly related to the nature of the cations in this limited study. For the diprotic [DBAH]$^+$ salts **2**, **4**, and **6**, the melting points are similar (97.0–98.3 °C) but their solidification behavior is distinctly different. **2** shows large supercooling, **4** does not recrystallize at all, and **6** recrystallizes readily. In comparison, the [Et$_3$NH]$^+$ salt **1** is a liquid while **3** and **5** melt at lower temperatures (78.6 °C and 33.8 °C, respectively) and do not recrystallize under the experimental conditions, rather exhibiting glass transitions around −40.2 °C and −40.8 °C, respectively.

3.3 Crystal structures

SCXRD confirms full proton transfer from the thiol to the amine and formation of the respective ammonium cation and azole thiolate anion in each salt. For all solid compounds (**2–6**), crystals of sufficient quality for SCXRD could be grown by isothermal evaporation of solutions in either methanol (**2–4**) or ethyl acetate (for the [MeDiTS]-based compounds **5** and **6**). Compounds **2–5** crystallize with one cation and one anion in the asymmetric unit and compound **6** – with two formula units. To fully assess any interactions that are important in the context of anti-crystal engineering, first, the structures of the individual ions as observed in the

Table 1 Melting points and decomposition temperatures for **1–6**

	Compound	Melting point (T_m, °C)	Crystallization (T_{cryst}, °C)	Glass transition (T_g, °C)	Decomposition temperature ($T_{5\%onset}$, °C)
1	$[Et_3NH][MeTzS]$	51.2[a]	NA	−56.9	164
2	[DBAH][MeTzS]	97.0	29.8	NA	122
3	$[Et_3NH][PhTzS]$	78.6	NA	−40.2	126
4	[DBAH][PhTzS]	97.8	NA	−15.0	127
5	$[Et_3NH][MeDiTS]$	33.8	NA	−40.8	164
6	[DBAH][MeDiTS]	98.3	89.9	NA	169

[a] Estimated according to $T_m = 1.5\ T_g$ (K).

structures will be discussed in the context of the respective counterion, and then the crystal packing will be analyzed.

The cations. Overall, the $[DBAH]^+$ cations in **2**, **4**, and **6** (Fig. 3) appear to be less affected by the type of anion always featuring a *cis* conformation with respect to the NH_2 group. The nearly planar mutual orientation of the isobutyl groups can be attributed to an indirect influence of the anions or, in a broader perspective, unique interaction between the cation and the anion in those salts. There are, however, some more subtle differences as the isobutyl chain planes form dihedral angles of 16.8(1), 26.8(1), and 18.3–21.2(1)°, respectively. In reported structures containing this cation but other anions, this angle has been observed in a much broader range of up to 90°.[38,39] Minor positional disorder was observed for one of the cations in the crystal structure of **6**, affecting mostly the C12′ position and C12′–H12′ orientation (*cis*/*trans* with respect to C12–H12). It is also worth noting that in **2**, C12–H12/C12′–H12′ mutual orientation is solely *cis*, while in **4** – *trans*, pointing no strong structural preference of the cation itself.

The conformationally flexible $[Et_3NH]^+$ cations do exhibit differences depending upon the anion or more precisely, their mutual orientation to optimize the packing (Fig. 3). The ethyl groups in **3** are T shaped with ∠C12N11C12′, ∠C12″ N11C12′ and ∠C12N11C12″ of 92.2(1), 94.2(1), and 172.8(1)°, while in **5**, the shape approaches an equilateral triangle with the angles 104.19(7), 125.13(7), and 119.19(7)°, respectively.

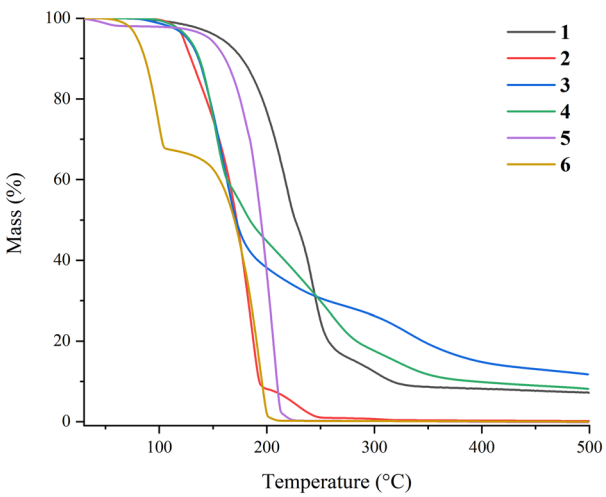

Fig. 2 TGA curves of **1–6**.

$[Et_3NH]^+$ cations in both **3** and **5** are, in general, in similar conformations as one would expect from these types of molecules within the expected variations.[38,40–42]

The anions. Compared to the cations, the anions in **2–6** (Fig. 4) exhibit less structural flexibility mainly due to their higher structural rigidity. In general, structures are on par with that reported in the literature previously for salts containing these anions.[43–46] All intra-ring angles are regular and never exceed 104–112(1)° (Table S1†), being very similar to the neutral 1-methyl-1*H*-tetrazole-5-thiol.[47]

The phenyl groups in **3** and **4** are responsible for a slight distortion of the azole ring that can be followed by the C–N and N–N bond variations. The tetrazole and phenyl ring of the anion exhibit an angle between them, 47.7(1)° in **3** and 46.6(1)° in **4**, showing a minor response to the cation variation.

The azole rings in **5–6** are significantly more distorted (the C–S–C angles in the latter are in the range 88.0–88.8(2)°) that is directly related to the incorporation of a larger S atom directly in the ring. These values are similar to the free 5-methyl-1,3,4-dithiazole-2-thiol (90.0°),[48] or for example, in a mixed phenyl phosphate complex of Cu^I (90.2°).[49]

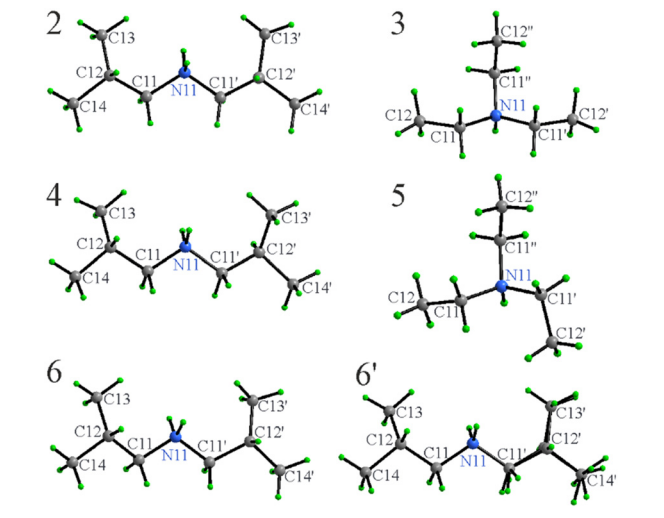

Fig. 3 Molecular structures and atom label assignments for cations in **2–6**. The second unique cation in the asymmetric unit of **6** (**6′**) is disordered (shown) with position C12′ split into two nearly identically occupied positions. Note the different conformations of the cations in **3** and **5**.

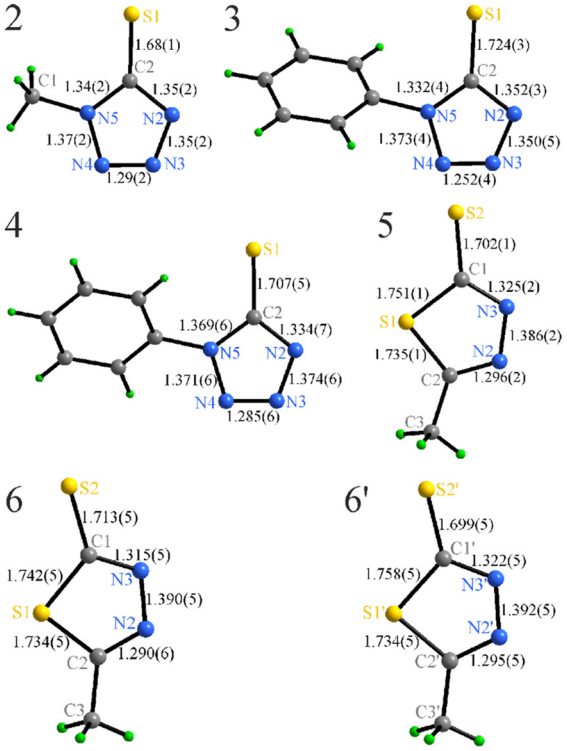

Fig. 4 Bond lengths (Å) within the anions in **2–6**.

The anions in **2–4** appear to be moderately affected by both the type of cation and the R-group substitution, showing minor elongation of the C2–S1 bond, shortening of the N3–N4 contacts, and slight redistribution of the intra-ring angles (Fig. 4, Table S1†).

Hydrogen bonding and supramolecular motifs. Hydrogen bonding has been invoked as the explanation for many of the unique properties of many ILs,[50] and it does seem to play a major role in the structures of **2–6**. The major interactions are charge-assisted N–H···N and N–H···S hydrogen bonds of various strengths (Table 2). There are also possible C–H···S contacts, particularly in **6**; however, most of them significantly exceed reasonable bonding ranges and will not be considered in detail here.

The $[DBAH]^+$ salts **2**, **4**, and **6** present extended hydrogen-bonded motifs, including solely N–H···N connectivity in **2** and mixed N–H···N and N–H···S in **4** and **6** (Fig. 5). The presence of two N–H donors in this cation results in motifs that extend in space and are represented by zigzag chains in all structures with coplanar azole rings. Additionally, weaker C–H···S connectivity (d_{H-S} = 2.695(1) Å) in **6** between the chains leads to the formation of formal layers, where azole rings in a given hydrogen-bonded chain belong to the same plane, while the azole rings in neighboring chains belong to parallel planes.

The situation in the $[Et_3NH]^+$ salts **3** and **5** is different. The number of N–H donors is limited to one, and the formation of extended motifs is geometrically blocked, resulting in hydrogen bonded ion pairs with either weaker N–H···S (**3**, Fig. 6) or stronger N–H···N (**5**) interactions. In **3**, the N–H···S hydrogen bond is of moderate strength at 2.540(3) Å,[51,52] however, there are other significant interactions. Although π–π stacking is not observed, the C11–H···π and C12″–H···π contacts are relatively short (2.72(1) and 2.82(1)) Å (Fig. 6), leading to the formation of a rather uniform network. This motif alternates 2-side C–H···π stacking and N–H···S hydrogen bonding, so each anion is connected to three cations while each cation connects to two anions.

Since the positions of the cations in **3** and **5** are restricted due to interaction with the phenyl ring, it is not surprising that the thiol S atom wins the competition for the N–H-bond donor. Overall, the system sacrifices potentially stronger N–H···N connectivity towards the strength-wise uniform combination of N–H···S and C–H···π, finally resulting in a higher melting point. Interestingly, **5** also exhibits a similar layered structure, though, in contrast to **3**, there are strong directional N–H···N bonds (1.820(2) Å). On the other hand, the C12–H···π in **5** connections involving the azole ring are slightly longer (weaker) (2.85–2.88(3) Å).

Hirshfeld surface analysis. A Hirshfeld surface analysis[53] was performed on **2–6** to obtain 2D fingerprints of the intermolecular interactions and to quantify the interaction distribution in the structures (Table S2†).[54–56] The fingerprint plots[57] are shown in Fig. 7 while the element specific

Table 2 Distances (Å) and angles (∠, °) of hydrogen bonds in the crystal structures of **2–6**

	2		**3**		**4**		**5**		**6**	
Type	*d*	∠	*d*	∠	*d*	∠	*d*	∠	*d*	∠
N11(H)···N2	2.84(1)				2.850(6)					
H···N2	1.93(1)				1.979(4)					
∠N11–H–N2		178.0(6)				159.6(3)				
N11(H)···N3	2.95(1)						2.738(2)		2.782(5)	
H···N3	2.04(1)						1.820(2)		1.872(4)	
∠N11–H–N3		177.6(7)						174(2)		177.9(3)
N11(H)···S1			3.265(3)		3.296(4)				3.257(4)	
H···S1			2.540(3)		2.432(1)				2.386(1)	
∠N11–H–S1				149(3)		158.6(2)				150.4(2)
C11(H)···S2									3.601(5)	
H···S2									2.695(1)	
∠C11–H–S2										152.3(3)

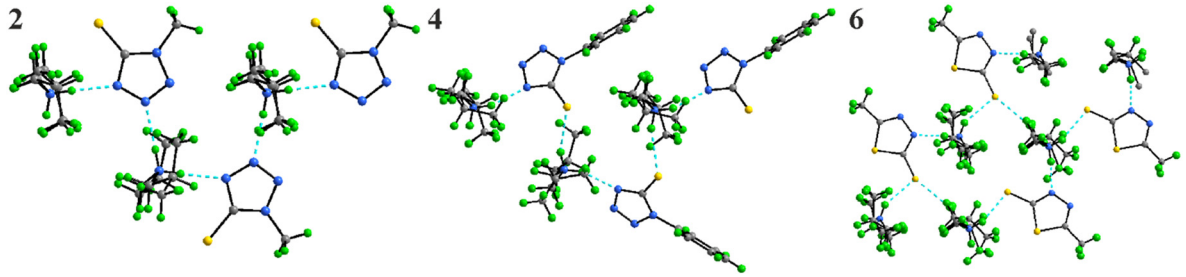

Fig. 5 Hydrogen-bonded (dotted blue) motifs in the crystal structures of **2**, **4**, and **6**.

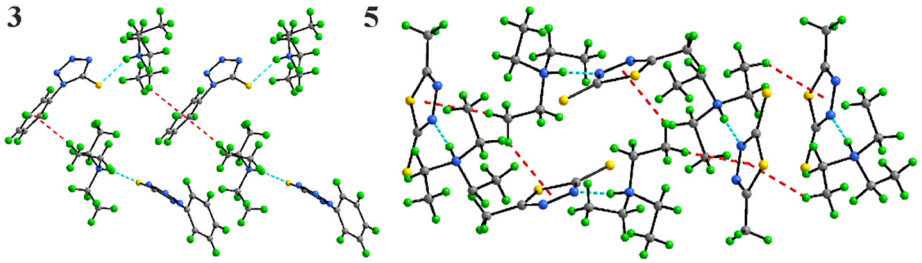

Fig. 6 Hydrogen bonded (dotted blue) ionic pairs in the crystal structures of **3** and **5**. C–H···π connectivity in **3** is indicated with dotted red lines.

fingerprints and the Hirshfeld surfaces mapped with the normalized contact distance d_{norm} and the shape index have been provided in Fig. S47–S50.† The values d_e refer to the distance from the Hirshfeld surface to a nucleus outside and

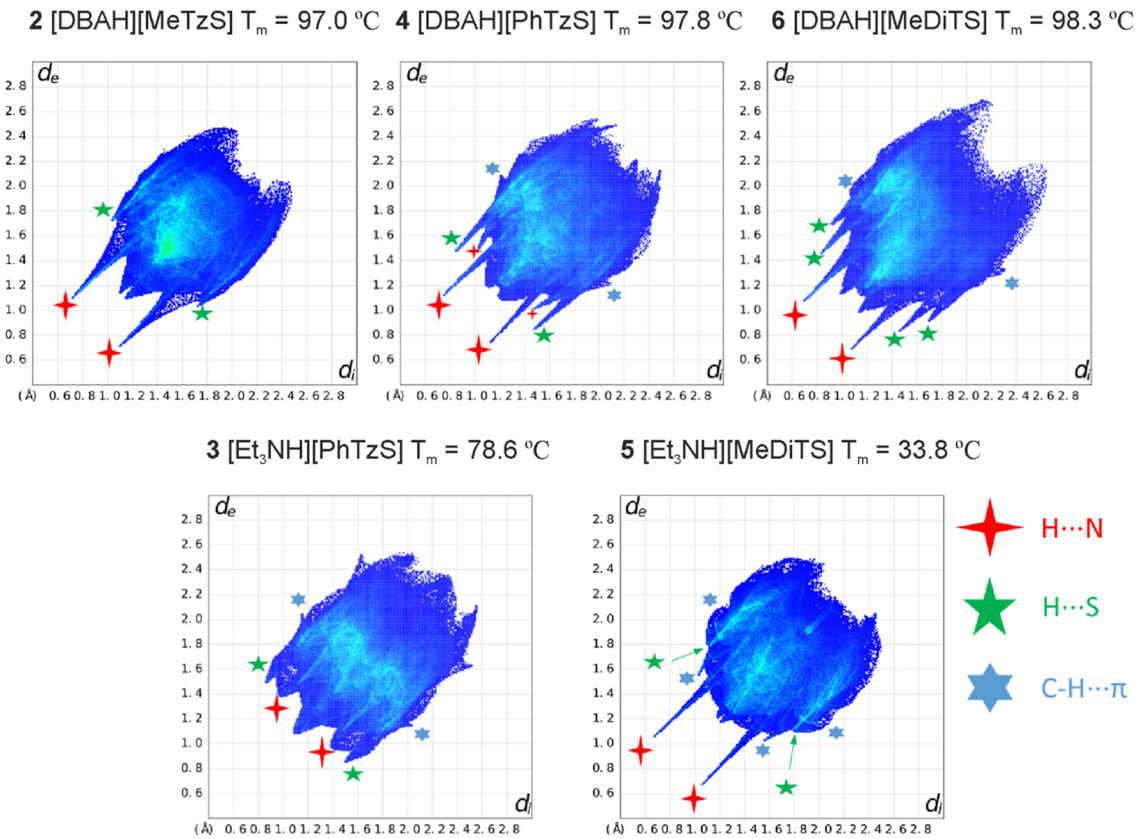

Fig. 7 2D fingerprints derived from the Hirshfeld surfaces showing the different types of intermolecular interactions dominating in each compound.

d_i to the distance to a nucleus inside. The sum of the two values gives the total distance of the interaction.[58]

It can be noted that the general shape of the fingerprints seems to be mainly dependent on the cation, indicating similar intermolecular interactions for similar cations. Another striking feature is the clear presence of the H···N interactions between the cation and the thiol ring (characterized by sharp spikes denoted with a red star) in all molecules except of **3**. One should also note that the H···S interactions (denoted with a green star) appear to be more prominent in **3**, **4**, and **6** with no direct relation to the type of the cation. In addition, and expectedly, H···C interactions are well represented in the two compounds containing $[PhTzS]^-$ (**3**–**4**) and $[MeDiTS]^-$ (**5**–**6**) as they exhibit noticeable C–H···π interactions (characterized by a "wing" in the fingerprint).

Packing. It is not surprising that despite somewhat different connectivities, many compounds exhibit packing motifs that are reminiscent of classical salt packing. On the other hand, each structure can be represented as stacking of formal layers (Fig. 8–10). The neighboring layers are shifted with respect to each other in order to maximize the amount of cation–anion bonding. For example, stacking in **2** represents a slightly distorted variant of the NaCl type of packing with checkered cations and anions along the main crystallographic directions (Fig. 8). Each cation is surrounded by six anions in octahedral coordination and *vice versa* (Fig. S37†). Essentially, a very similar alternation was also observed in **3** and **5**, with specifics leading to some angles between the propagation directions being different from 90° (Fig. 9) but keeping identical octahedral coordination, though with different degrees of distortion. The packings in **4** and **6** differ significantly from **2**, **3**, or **5** as together with standard cation–anion alternation along the single direction (*c* and *b*, respectively) they allow global segregation or local domains of unpolar parts with preferably van der Waals connectivity (Fig. 10). Both structures can be represented as bilayered. Particularly in **6**, the cations and the anions stack pairwise along the *b* axis, leading to a very clear separation. This segregation and bilayered motifs in **4** are slightly less evident as the anions exhibit different orientations leading to a more efficient packing in a single layer, while the cations form zigzag motifs, again leading to a more efficient stacking with the anionic layers. In addition to the coulombic interactions, the anions in the crystal packing of **2** make short contacts to five neighboring cations, in **3** –to five cations and three anions, in **4** – to five cations, in **5** – with five cations and one anion, and **6** – to four cations (Fig. S40 and S41†).

Bonding *vs.* thermal behavior. The connectivity of the ions in each structure, particularly the charge-assisted hydrogen bonding, correlates well with the observed melting behavior. The three salts of the slightly smaller cation, $[Et_3NH]^+$, with only one potential charge assisted N–H hydrogen bond donor, exhibited the lowest melting points, including the room temperature IL **1**. Even though **3** has only a moderate N–H···S hydrogen bond, the packing, which results in significant interactions with the phenyl ring, leading to the highest melting point of these three salts (78.6 °C). **5** melts just above room temperature (33.8 °C), despite having a stronger N–H···N hydrogen bond.

All three diprotic $[DBAH]^+$ salts (**2**, **4**, and **6**) with two charge assisted N–H hydrogen bonds exhibit seemingly more ordered structures. The variety of hydrogen-bond interactions further translates into the packing diagram of the ILs, with similar zigzag patterns being exhibited according to the cation present in the molecule. Given their broad connectivity, it is understandable that these have the highest and similar melting points (all above 95 °C) of the salts studied here.

The decomposition temperatures seem to be dependent on the anion's identity rather than the connectivity between the ion pairs. In fact, both compounds **3** and **4** and compounds **5** and **6**, respectively, composed of $[PhTzS]^-$ and $[MeDiTS]^-$ exhibit decomposition temperatures within a couple of degrees from each other (126 ± 1 °C for **3** and **4** and 166 ± 3 °C for **5** and **6**). However, the highest decomposition temperatures are also exhibited by the compounds displaying the strongest contribution of the N–H···S bond.

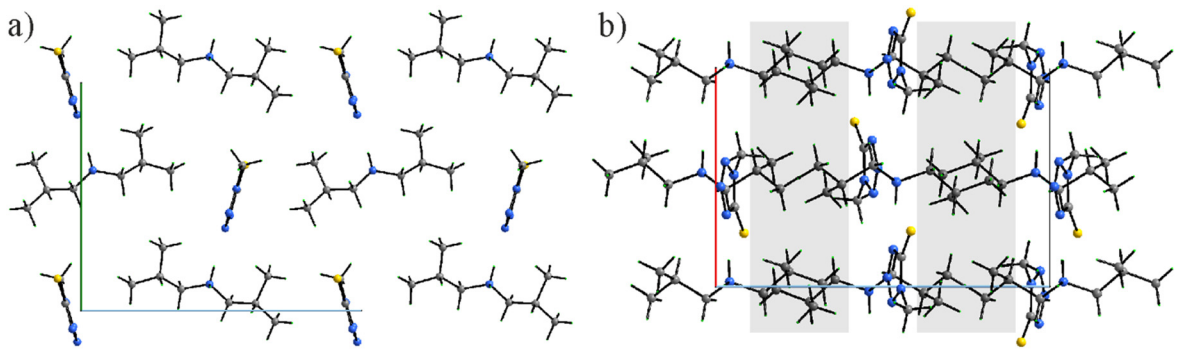

Fig. 8 Projection of a single layer in the crystal structures of **2** on the *bc* plane (a) and the crystal packing on the *ac* plane (b). Apolar segments have been highlighted. Crystallographic axes are color-coded: *a* = red, *b* = green, *c* = blue.

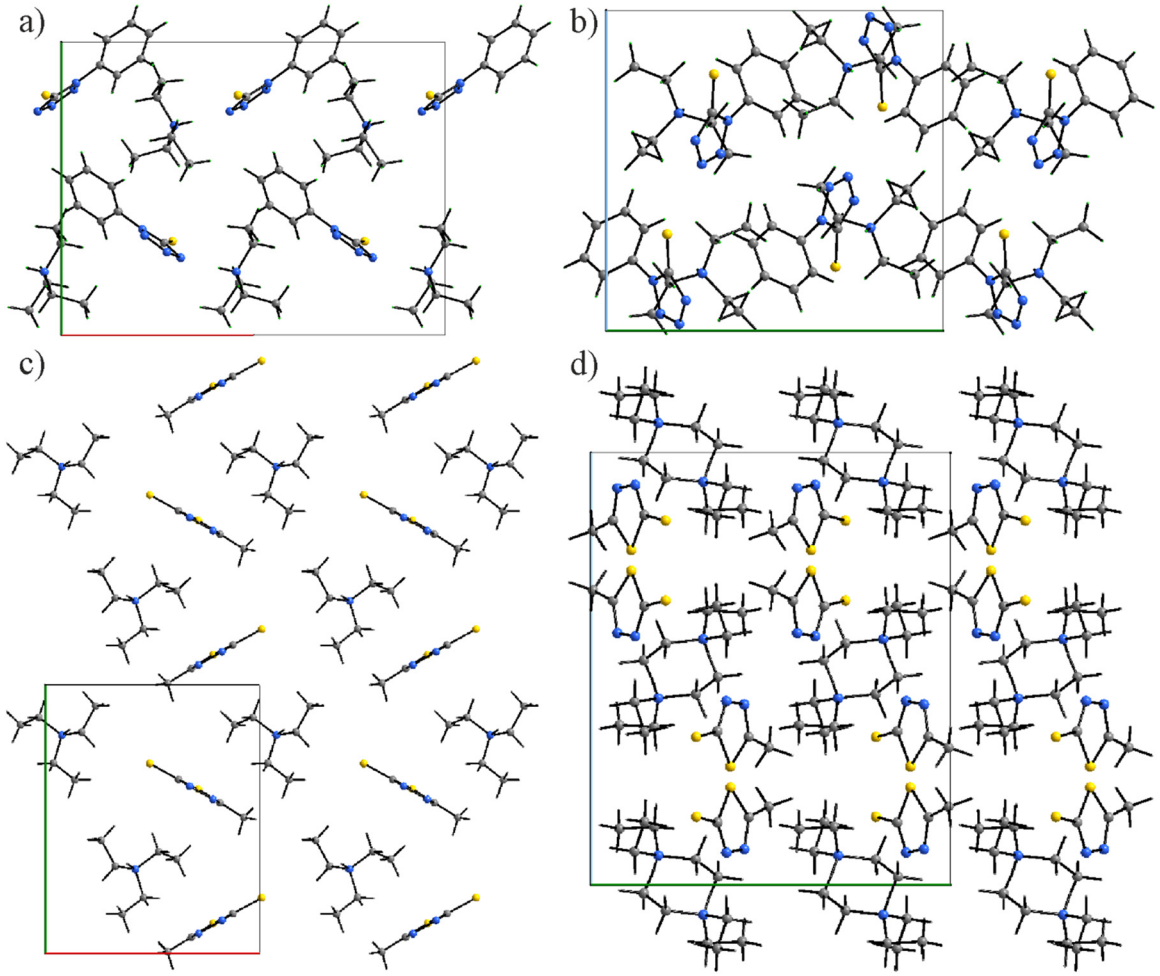

Fig. 9 Projection of a single layer in the crystal structures of **3** and **5** on the *ab* plane (a and c, respectively) and the crystal packing on the *bc* plane (b and d, respectively). Crystallographic axes are color-coded: *a* = red, *b* = green, *c* = blue.

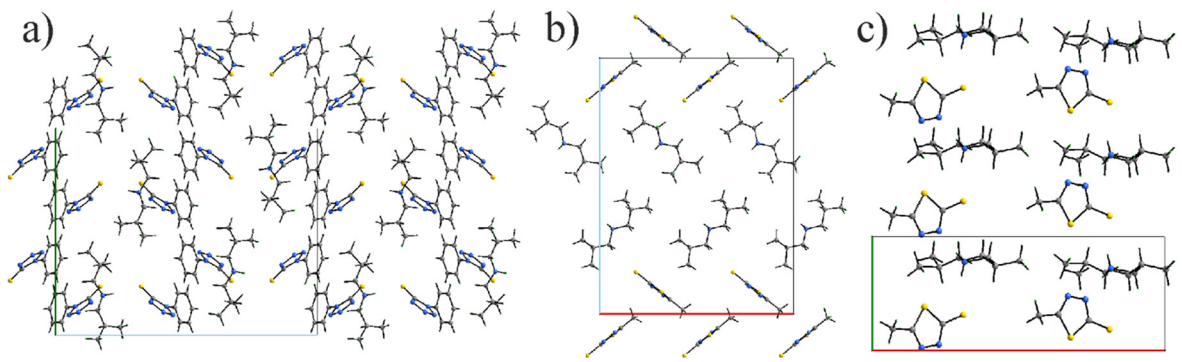

Fig. 10 Projection of a single layer in the crystal structures of **4** on the *bc* plane (a), of **6** on the *ac* plane (b) and the crystal packing of **6** on the *ab* plane (c). Crystallographic axes are color-coded: *a* = red, *b* = green, *c* = blue.

Conclusions

Six new ILs, including one room temperature IL, containing both N- and S-donors, have been synthesized and characterized. The crystal structures of the five crystalline solids reveal extensive hydrogen bonded networks that are cation dependent. Three of the compounds (**3**, **4**, and **6**) present relatively rare charge assisted N–H···S hydrogen bonds. While C–H···π interactions are present in nearly all these salts, it plays a supportive role in those with strong N–H···S hydrogen bonding. By contrast, C–H···π interactions appear to be the main driving force in the thermal behavior of **3**. Although hydrogen bonding is important in these salts, there does not seem to be one type, which can be assigned as

the major driver for the observed physical properties of a given IL, but rather the combination of multiple intermolecular interactions. These dissimilarities can easily be observed from the Hirshfeld surface fingerprints between **3** and **5**, directly pointing to different connectivities in the solid state.

The thermal behavior of $[DBAH]^+$ salts is strongly dictated by polymeric hydrogen bonded motifs leading to higher melting points, while $[Et_3NH]^+$ salts allow stronger competition between different types of bonding and show higher differentiation of their melting temperatures. Even the limited set of investigated compounds suggest that control of the hydrogen bond network could be a tool for designing the ILs' properties. Future research will be focused on the correlation between the specific structural features, hydrogen bonding, and the resulting physico-chemical characteristics to allow fine tuning towards desired properties and will consequently lead to further expansion of the library of task specific ILs.

Author contributions

OR, GB: methodology, investigation, writing. VS: analysis, writing, visualization. AVM, RDR: conceptualization, supervision, analysis, writing, funding support.

Conflicts of interest

The authors declare no competing financial interest.

Acknowledgements

A.-V. M. would like to thank the Royal Academy of Sciences, Sweden, for support through the Göran Gustafsson prize in Chemistry, Energimydigheten (The Swedish Energy Agency) for support through grant no. 46676-1 and Stiftelsen för Strategisk Forskning (Swedish Foundation for Strategic Research, SSF) for support in the REFIT research consortium. A.-V. M. and R. D. R. acknowledge the Swedish Research Council for a Tage Erlander professorship to R. D. R. (VR grant 2018-00233). R. D. R would like to thank the U.S. Department of Energy, Office of Science, Office of Basic Energy Sciences, Heavy Elements program for support under award DE-SC0019220.

References

1 L. Mei, P. Ren, Q.-Y. Wu, Y.-B. Ke, J.-S. Geng, K. Liu, X.-Q. Xing, Z.-W. Huang, K.-Q. Hu, Y.-L. Liu, L.-Y. Yuan, G. Mo, Z.-H. Wu, J. K. Gibson, Z.-F. Chai and W.-Q. Shi, *J. Am. Chem. Soc.*, 2020, **142**, 16538–16545.
2 F. W. Lewis, L. M. Harwood, M. J. Hudson, M. G. B. Drew, J. F. Desreux, G. Vidick, N. Bouslimani, G. Modolo, A. Wilden, M. Sypula, T.-H. Vu and J.-P. Simonin, *J. Am. Chem. Soc.*, 2011, **133**, 13093–13102.
3 C. Xiao, Z. Hassanzadeh Fard, D. Sarma, T.-B. Song, C. Xu and M. G. Kanatzidis, *J. Am. Chem. Soc.*, 2017, **139**, 16494–16497.
4 D. Prodius, M. Klocke, V. Smetana, T. Alammar, M. Perez Garcia, T. L. Windus, I. C. Nlebedim and A.-V. Mudring, *Chem. Commun.*, 2020, **56**, 11386–11389.
5 D. Prodius, K. Gandha, A.-V. Mudring and I. C. Nlebedim, *ACS Sustainable Chem. Eng.*, 2020, **8**, 1455–1463.
6 A. V. Rudnev, *Russ. Chem. Rev.*, 2020, **89**, 1463.
7 J.-C. G. Bünzli, *Trends Chem.*, 2019, **1**, 751–762.
8 D. Prodius and A.-V. Mudring, *Coord. Chem. Rev.*, 2018, **363**, 1–16.
9 X. Sun, H. Luo and S. Dai, *Chem. Rev.*, 2012, **112**, 2100–2128.
10 A. P. Abbott, G. Frisch, J. Hartley and K. S. Ryder, *Green Chem.*, 2011, **13**, 471–481.
11 I. Billard, in *Handbook on the Physics and Chemistry of Rare Earths*, ed. J.-C. G. Bünzli and V. K. Pecharsky, Elsevier, 2013, vol. 43, pp. 213–273.
12 A. Rout and K. Binnemans, *Dalton Trans.*, 2014, **43**, 3186–3195.
13 M. P. Jensen and A. H. Bond, *J. Am. Chem. Soc.*, 2002, **124**, 9870–9877.
14 A. Bhattacharyya, P. Mohapatra and V. Manchanda, *J. Radioanal. Nucl. Chem.*, 2011, **288**, 709–716.
15 V. A. Cocalia, M. P. Jensen, J. D. Holbrey, S. K. Spear, D. C. Stepinski and R. D. Rogers, *Dalton Trans.*, 2005, 1966–1971.
16 S. P. Kelley, J. S. Nuss and R. D. Rogers, in *Application of Ionic Liquids on Rare Earth Green Separation and Utilization*, ed. J. Chen, Springer, Heidelberg, 2016, pp. 21–42.
17 X. Han and D. W. Armstrong, *Acc. Chem. Res.*, 2007, **40**, 1079–1086.
18 L. Xu, N. Pu, Y. Li, P. Wei, T. Sun, C. Xiao, J. Chen and C. Xu, *Inorg. Chem.*, 2019, **58**, 4420–4430.
19 S. Laufer, G. Wagner and D. Kotschenreuther, *Angew. Chem., Int. Ed.*, 2002, **41**, 2290–2293.
20 M. E. Easton, H. Choudhary and R. D. Rogers, *Chem. – Eur. J.*, 2019, **25**, 2127–2140.
21 D. M. S. Paqhaleh, L. Hashemi, V. Amani, A. Morsali and A. Aminjanov, *Inorg. Chim. Acta*, 2013, **407**, 1–6.
22 M. Taheriha, M. Ghadermazi and V. Amani, *J. Mol. Struct.*, 2016, **1107**, 57–65.
23 W. Lu, P. S. Barber, S. P. Kelley and R. D. Rogers, *Dalton Trans.*, 2013, **42**, 12908–12916.
24 A. Marakushev and N. Bezmen, *Int. Geol. Rev.*, 1971, **13**, 1781–1794.
25 J. S. Preston and A. C. D. Preez, *Solvent Extr. Ion Exch.*, 1994, **12**, 667–685.
26 T. Vander Hoogerstraete, B. Onghena and K. Binnemans, *J. Phys. Chem. Lett.*, 2013, **4**, 1659–1663.
27 D. Yaprak, E. T. Spielberg, T. Bäcker, M. Richter, B. Mallick, A. Klein and A.-V. Mudring, *Chem. – Eur. J.*, 2014, **20**, 6482–6493.
28 P. M. Dean, J. Turanjanin, M. Yoshizawa-Fujita, D. R. MacFarlane and J. L. Scott, *Cryst. Growth Des.*, 2009, **9**, 1137–1145.
29 G. Sheldrick, *Acta Crystallogr., Sect. A: Found. Adv.*, 2015, **71**, 3–8.
30 G. Sheldrick, *Acta Crystallogr., Sect. C: Struct. Chem.*, 2015, **71**, 3–8.

31 Bruker AXS Inc., Wisconsin, USA, 2016.
32 L. Krause, R. Herbst-Irmer and D. Stalke, *J. Appl. Crystallogr.*, 2015, **48**, 1907–1913.
33 *DIAMOND: Program for Crystal and Molecular Structure Visualization*, Crystal Impact GbR, Bonn, Germany, 2011.
34 C. F. Macrae, P. R. Edgington, P. McCabe, E. Pidcock, G. P. Shields, R. Taylor, M. Towler and J. Streek, *J. Appl. Crystallogr.*, 2006, **39**, 453–457.
35 S. Wolff, D. Grimwood, J. McKinnon, M. Turner, D. Jayatilaka and M. Spackman, *Crystal explorer*, 2012.
36 A.-V. Mudring, *Aust. J. Chem.*, 2010, **63**, 544–564.
37 O. Renier, G. Bousrez, M. Yang, M. Hölter, B. Mallick, V. Smetana and A.-V. Mudring, *CrystEngComm*, 2021, **23**, 1785–1795.
38 A. Piecha-Bisiorek, A. Białońska, R. Jakubas, P. Zieliński, M. Wojciechowska and M. Gałązka, *Adv. Mater.*, 2015, **27**, 5023–5027.
39 A. Suvitha, B. Varghese and M. N. Sudheendra Rao, *Acta Crystallogr., Sect. E: Struct. Rep. Online*, 2006, **62**, o344–o346.
40 L. E. Shmukler, I. V. Fedorova, M. S. Gruzdev and L. P. Safonova, *J. Phys. Chem. B*, 2019, **123**, 10794–10806.
41 A. V. Churakov and J. A. Howard, *Acta Crystallogr., Sect. C: Cryst. Struct. Commun.*, 2004, **60**, o557–o558.
42 T. J. Bednarchuk, V. Kinzhybalo, E. Markiewicz, B. Hilczer and A. Pietraszko, *J. Solid State Chem.*, 2018, **258**, 753–761.
43 G. Liu and S. Zhang, *Z. Kristallogr. - New Cryst. Struct.*, 2016, **231**, 479–480.
44 O. Jiménez-Sandoval, R. Cea-Olivares and S. Hernández-Ortega, *Polyhedron*, 1997, **16**, 4129–4135.
45 M. Hernández-Arganis, R. A. Toscano, M. Moya-Cabrera, V. García-Montalvo and R. Cea-Olivares, *Z. Anorg. Allg. Chem.*, 2004, **630**, 1627–1631.
46 K. Ortner and U. Abram, *Polyhedron*, 1999, **18**, 749–754.
47 R. Cea-Olivares, O. Jiménez-Sandoval, S. Hernández-Ortega, M. Sánchez, R. A. Toscano and I. Haiduc, *Heteroat. Chem.*, 1995, **6**, 89–97.
48 F. Hipler, M. Winter and R. A. Fischer, *J. Mol. Struct.*, 2003, **658**, 179–191.
49 V. Stylidou, K. Kavaratzi, I. Papazoglou, A. G. Hatzidimitriou, A. G. Papadopoulos, P. Angaridis and P. Aslanidis, *Eur. J. Inorg. Chem.*, 2018, **2018**, 2915–2926.
50 P. A. Hunt, C. R. Ashworth and R. P. Matthews, *Chem. Soc. Rev.*, 2015, **44**, 1257–1288.
51 L. A. H. van Bergen, M. Alonso, A. Palló, L. Nilsson, F. De Proft and J. Messens, *Sci. Rep.*, 2016, **6**, 30369.
52 P. Zhou, F. Tian, F. Lv and Z. Shang, *Proteins: Struct., Funct., Bioinf.*, 2009, **76**, 151–163.
53 J. J. McKinnon, M. A. Spackman and A. S. Mitchell, *Acta Crystallogr., Sect. B: Struct. Sci.*, 2004, **60**, 627–668.
54 A. Parkin, G. Barr, W. Dong, C. J. Gilmore, D. Jayatilaka, J. J. McKinnon, M. A. Spackman and C. C. Wilson, *CrystEngComm*, 2007, **9**, 648–652.
55 M. A. Spackman and J. J. McKinnon, *CrystEngComm*, 2002, **4**, 378–392.
56 J. J. McKinnon, D. Jayatilaka and M. A. Spackman, *Chem. Commun.*, 2007, 3814–3816.
57 H. S. Biswal and S. Wategaonkar, *J. Phys. Chem. A*, 2009, **113**, 12763–12773.
58 M. A. Spackman and D. Jayatilaka, *CrystEngComm*, 2009, **11**, 19–32.

